ACS OMEGA

Article

Cite This: ACS Omega 2020, 5, 2123−2132

Pt-Ni@PC900 Hybrid Derived from Layered-Structure Cd-MOF for Fuel Cell ORR Activity

Muhammad Nadeem,[†,‡,∥,#] Ghulam Yasin,[‡,#] Muhammad Arif,[‡] Moazzam H. Bhatti,[*,†] Koray Sayin,[§] Mazhar Mehmood,[∥] Uzma Yunus,[†] Shoaib Mehboob,[∥] Imtiaz Ahmed,[†] and Ulrich Flörke[⊥]

[†]Department of Chemistry, Allama Iqbal Open University, Islamabad 44000, Pakistan

[‡]State Key Laboratory of Chemical Resource Engineering, Institute of Science, and College of Energy, Beijing University of Chemical Technology, Beijing 100029, P. R. China

[§]Department of Chemistry, Institute of Science, Cumhuriyet University, Sivas 58140, Turkey

[∥]National Center for Nanotechnology, Department of Metallurgy and Materials Engineering, Pakistan Institute of Engineering and Applied Sciences (PIEAS), Nilore, Islamabad 45650, Pakistan

[⊥]Anorganische und Analytische Chemie, Fakultät für Naturwissenschaften, Universität Paderborn, Warburgerstrasse 100, Paderborn D-33098, Germany

Supporting Information

ABSTRACT: Fuel cell technology is the supreme alternate option for the replacement of fossil fuel in the current era. Pt alloys can perform well as fuel cell electrodes for being used as catalytic materials to perform the very notorious oxygen reduction reaction. In this regard, first, a layered metal−organic framework with empirical formula $[C_8H_{10}CdO_7]_n \cdot 4H_2O$ is synthesized and characterized using various experimental and theoretical techniques. Then, a nanostructured porous carbon material with a sheet morphology (PC900) having a high BET surface area of 877 $m^2\ g^{-1}$ is fabricated by an inert-atmosphere thermal treatment of the framework upon heating up to 900 °C. Pt and Ni nanoparticles are embedded into PC900 to prepare a homogenized hybrid functional material, i.e., Pt-Ni@PC900. The Pt-Ni@PC900 hybrid is proved to be an excellent ORR catalyst in terms of half-wave potential and limiting current density with 7% Pt loading compared with the commercially available 20% Pt/C catalyst. Pt-Ni@PC900 also shows stability of current up to 12 h with only a very small variation in current. This work highlights the importance of Pt alloys in future large-scale commercial applications of fuel cells.

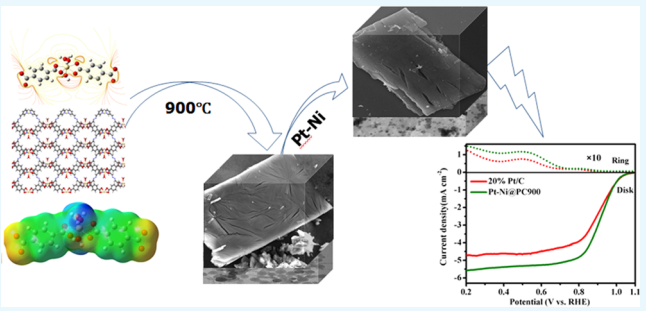

1. INTRODUCTION

A fuel cell is one of the renewable energy devices, and for its commercialization the main hurdle is the development of an economic, efficient, and durable catalyst that can perform the most vital oxygen reduction reaction (ORR).[1−6] Various Pt-based hybrid compounds have been utilized to perform the ORR, but still there are durability, efficiency, and economic problems.[7] The main challenge is to reduce the Pt content in the catalyst by coupling Pt with other cheap metals, such as Ni and Cu, along with a porous carbon material as a support.[8−11] Therefore, the role of a support in a catalyst to enhance its activity, stability, and durability is very vital.[12,13] Carbon-based fuel cell catalysts, whether they are used with carbon as a support or alone as catalysts, have shown impressive results.[14−17]

Metal−organic frameworks are very promising materials for important applications, such as in luminescence, optical sensors, and NLO materials.[18−21] Owing to the versatility, including porosity, surface area, electrochemical stability, and good electrical conductivity, of metal−organic framework-derived nanostructured carbon, it is reported as a good functional support for precious metal nanoparticles and alloys of nanoparticles to provide excellent electrocatalytic activity during electrochemical catalysis reactions.[22−27] These carbon-supported electrocatalysts have performed well in many electrocatalytic applications, such as the hydrogen evolution reaction, direct-methanol fuel cells, alkaline and acidic fuel cells, dehydrogenation processes for hydrazine, and oxidation of formic acid.[23−26,28]

Here, we have synthesized Cd-MOF crystals and characterized through single-crystal X-ray analysis. The computational study of the cadmium MOF is performed using the B3LYP/LANL2DZ level of theory in vacuum. Geometric parameters, and IR and UV−vis spectra are calculated and

Received: August 25, 2019
Accepted: December 6, 2019
Published: January 27, 2020

DOI: 10.1021/acsomega.9b02741
ACS Omega 2020, 5, 2123−2132

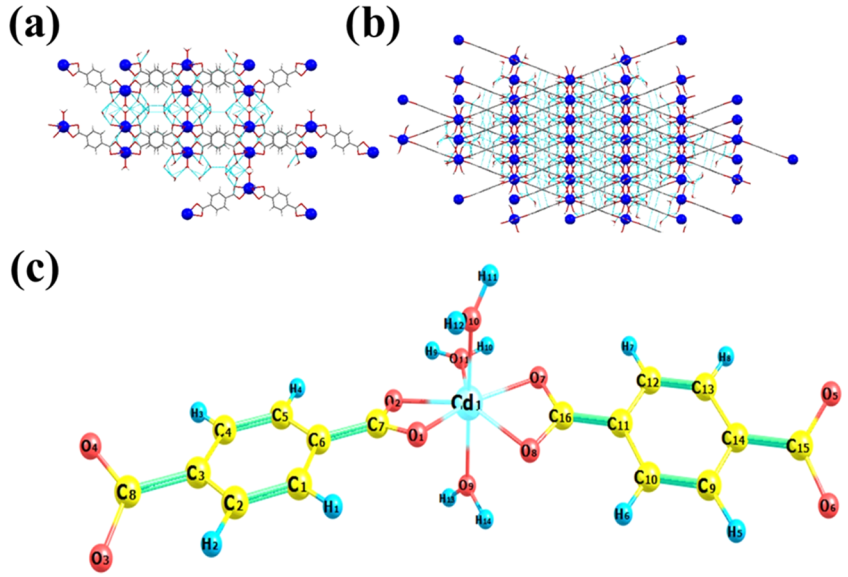

Figure 1. (a) Perspective view of the crystal structure of Cd-MOF along the *b*-axis (blue spheres show the Cd metal). (b) Extended two-dimensional framework structure of Cd-MOF (blue spheres show the Cd metal). (c) Optimized structure of the cadmium MOF at the B3LYP/LANL2DZ level in the gas phase (the atom name with number is given on the spheres; red color for oxygen, yellow color for carbon, blue color for hydrogen, and light blue color for Cd metal).

examined in detail. Also, its NLO properties are investigated at the same level of theory, and it is found that the NLO properties of the cadmium complex are better than those of urea. The framework was then sacrificed to obtain a nanostructured porous carbon material, which was utilized as a support to prepare a Pt-Ni@PC900 composite with 7% Pt loading. The synthesized composite was tested as an ORR catalyst for alkaline fuel cells. The results in terms of the onset potential, half-wave potential, limiting current density, and accelerating durability test were compared with those of the 20% Pt/C catalyst.

2. RESULTS AND DISCUSSION

2.1. Structural Details. Yang et al. proposed the theoretical quantum mechanical properties of Cd-MOF-5 by considering its similarity with Zn-MOF-5 due to the same linker molecule,[29] while the reported Cd-MOF[30,31] with a H_2BDC linker was different from the proposed structure of Cd-MOF-5. An effort was made to achieve the desired structure, as claimed. Different synthetic protocols were adopted to find the structure, as claimed, i.e., Cd-MOF-5. But our experimental finding was also the same as that reported but with a small variation in the synthesis scheme. One advantage was that in previous schemes DMF was used,[32,33] whereas in our synthetic route, it was completely hydrothermal; hence, toxic DMF was avoided, and the yield was also improved through temperature, time, sonication, and heating rate control. The compound, $(C_8H_{10}CdO_7)_n{\cdot}4H_2O$, crystallized in an orthorhombic system with the *Pcca* space group. Each Cd atom is coordinated to three water molecules and two carboxylate oxygen in a chelating manner, generating a 2D coordination chain, as shown in Figure 1a. The crystal refinement details are given in Table S1. The extended two-dimensional structure of the compound is presented in Figure 1b.

The Cd compound was optimized at the B3LYP/LANL2DZ level in the gas phase, and the optimized structures are displayed in Figure 1c with atomic labeling. The Cd metal atom is surrounded by seven coordinate covalent bonds formed by the oxygen atoms labeled O1, O2, O7, O8, O9, and O10, related to two BDC^{-2} ligands and three water molecules. Four oxygen atoms (O1, O2, O7, and O8) of the two BDC^{-2} linkers and one oxygen atom O11 of a water molecule are present in the equatorial positions, while the remaining two oxygen atoms (O9 and O10) belonging to the remaining two water molecules are in the axial positions. The selected theoretical and experimental structural parameters of the studied Cd-MOF are given in Table S2. The theoretical bond lengths for Cd-O1 and Cd-O2 related to one BDC^{-2} linker are 2.057 and 2.061 Å, while the corresponding experimental bond lengths are 2.500 and 2.357 Å, respectively. The calculated bond lengths of the second BDC^{-2} ligand for Cd-O7 and Cd-O8 are 2.046 and 2.049 Å, while the corresponding experimental bond distances are the same as for Cd-O1 and Cd-O2. The experimental and theoretical measurements for the Cd-O bond related to both BDC^{-2} ligands connected to one Cd metal in the framework showed agreement with a small variation. The Cd-O bond lengths for the three coordinated water molecules were found to be in the ranges 2.041−2.050 and 2.236−2.250 Å theoretically and experimentally, respectively. The reported experimental and theoretical Cd-O bond length for a seven-coordinated Cd complex system lie in the range 2.332−2.648 Å, which match well with those for the Cd coordination polymer in this study.[34−36] The bond angles calculated through DFT calculations for O1-Cd1-O2, O7-Cd1-O8, O1-Cd1-O9, and O7-Cd1-O11 are 63.6, 63.9, 92.4, and 74.7° that show variations with the corresponding experimental values of 53.79, 53.79, 88.37, and 82.66°, respectively. According to Table S2, bond lengths between the metal and donor atoms are close to 2 Å. The bond angle among O9, Cd1, and O10 is equal to 168.3°, justifying the axial positions. Additionally, the sum of angles in the equatorial position (O1-Cd1-O2, O2-Cd1-O11, O1-Cd1-O8, O7-Cd1-O8, and O7-Cd1-O11) is equal to 363.7°. The geometric structure of a related compound is a distorted pentagonal bipyramid. As for the dihedral angles, these angles imply that there is generally a

DOI: 10.1021/acsomega.9b02741
ACS Omega 2020, 5, 2123−2132

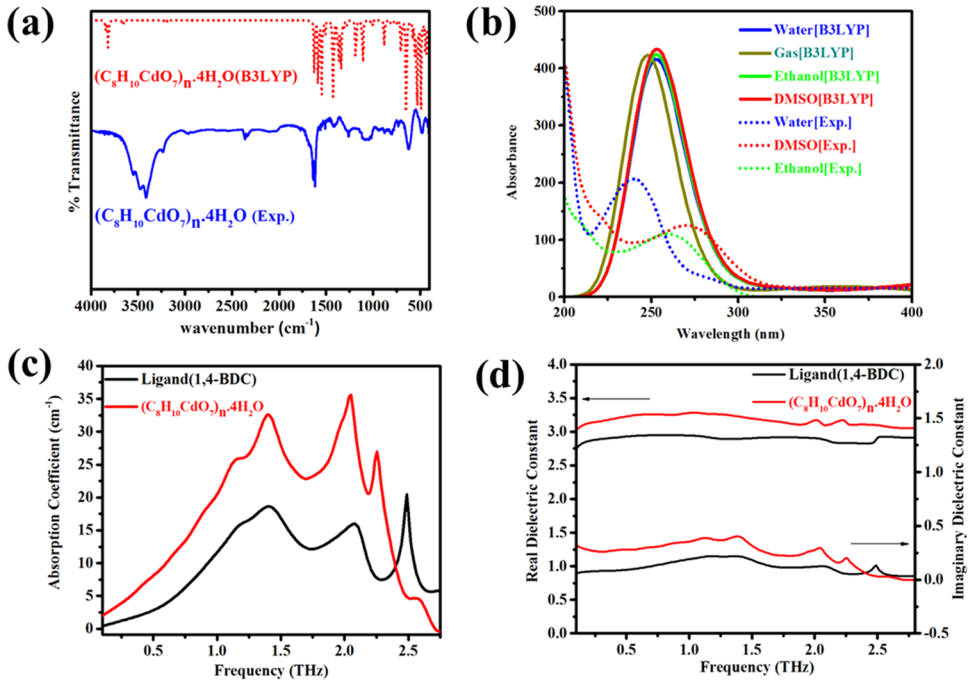

Figure 2. (a) Experimental and calculated FTIR spectra of Cd-MOF at the B3LYP/LANL2DZ level. (b) Experimental and calculated electronic absorption spectra in the ground state of Cd-MOF at the TD-B3LYP/LANL2DZ level in the gas phase and the TD-B3LYP/LANL2DZ-CPCM level in water, ethanol, and DMSO. (c) Absorption coefficient of Cd-MOF and H_2BDC measured using THz-TDS. (d) Real and imaginary parts of the dielectric constant of Cd-MOF and H_2BDC measured using THz-TDS.

planarity in the molecule. The Cd metal−organic framework is layered, and each layer is connected with the other one through hydrogen bonds.[31]

2.2. FTIR and Theoretical IR Spectroscopy of Cd-MOF. FTIR and theoretical IR spectra of Cd-MOF are presented in Figure 2a. The detailed peak positions with suitable assignment of bonds derived from spectral results are given in Table S3. The medium broad absorption bands in the experimental spectrum of Cd-MOF at 3556, 3474, and 3414 cm^{-1} are related to the existence of coordinated water molecules.[37,38] Similar bands for O−H asymmetric and symmetric stretches in the calculated spectrum are located at 3750 and 3600 cm^{-1}, respectively. The stretching vibrations for C═C appear at 1616 cm^{-1} in the experimental spectrum, while the theoretical assignment for the said vibrations is at 1598 cm^{-1}. The asymmetric and symmetric stretching bands for COO^{-1} are present at 1498 and 1267 cm^{-1} in the experimental spectrum, respectively. These vibrations in the calculated spectrum are found at 1424 and 1186 cm^{-1}, respectively. The frequency gap between these two stretches provides information about the coordination modes of the ligand with metal.[39−41] The coordination mode for one BDC^{-2} is tetradentate. The C−O stretching vibrations lie at 1410 and 1430 cm^{-1} in experimental and theoretical infrared spectra, respectively. The Cd−O bond vibrations are present at 643 and 487 cm^{-1} in theoretical calculations, while in experimental findings the Cd−O bond vibrations are exhibited at 621 and 481 cm^{-1}.

2.3. Electronic Transitions and Surface Properties of Cd-MOF. The calculated electronic absorption spectra of Cd-MOF at the TD-B3LYP/LANL2DZ and TD-B3LYP/LANL2DZ-CPCM levels along with the experimental spectra are shown in Figure 2b. The theoretical results for the gas phase, water, ethanol, and DMSO are 248 nm (ε = 1), 250 nm (ε = 78.3553), 251 nm (ε = 24.852), and 251 nm (ε = 46.826), respectively. The experimental maximum wavelengths for water, ethanol, and DMSO are at 240 nm (ε = 450), 261 nm (ε = 347), and 272 nm (ε = 321), respectively. The maximum wavelength associated with all solvents corresponds to $\pi-\pi^*$ transitions.[42] The theoretical results show that energy differences between frontier molecular orbitals are similar to each other in each area. Therefore, freedom of electron movement is similar to each other in each area.

By utilizing theoretical calculations, active sites of the Cd organic framework are analyzed here to elucidate the mechanistic path for the reaction of the title MOF. The mentioned active sites can be proposed via molecular electrostatic potential (MEP) surfaces, MEP contours, frontier molecular orbitals (FMOs) and energy diagrams. In this study, the energy diagrams of molecular orbitals are examined, and contour diagrams of frontier molecular orbitals, which are HOMO and LUMO, are calculated and presented in Figure S1. The energy of LUMO is 7.224×10^{-2} eV, while HOMO has an energy of 7.847×10^{-2} eV. The energy gap between the HOMO and LUMO is 0.623 eV. The low energy gap between the LUMO and HOMO provides information about the reactivity of the complex molecule. The contour diagram for the highest occupied molecular orbital (HOMO) and the lowest unoccupied molecular orbital (LUMO) is calculated by considering the fact that there are no co-energetic orbitals around the HOMO and LUMO. It can be concluded that the electrons of the HOMO are mainly localized on the outermost oxygen atoms, while for the LUMO, if the studied framework accepts electrons, the electrons are mainly delocalized on the structure. Additionally, MEP maps and contour diagrams for molecular orbitals for Cd-MOF are calculated and presented in Figure S2. According to the MEP map shown in Figure S2, the most active region or site is the environment around the outermost oxygen atoms. The active region is indicated by the

DOI: 10.1021/acsomega.9b02741
ACS Omega 2020, 5, 2123−2132

red and yellow colors in the MEP map. The negative charge is concentrated around the oxygen atom.

2.4. THz Spectroscopy Measurements. The terahertz time-domain (THz-TD) spectroscopy is very useful to study low-frequency vibrations, which are very important for determining the lattice dynamics that will decide the breathing phenomenon of metal−organic frameworks for absorption and release of radiation, and it also provides information about the stability of the frameworks.[43,44] Terahertz (10^{12} hertz = 1 THz) light, which is the intermediate region between microwaves and infrared waves, has been used for the investigation of water hydration dynamics with the MOF-5 material.[45] This powerful technique is useful to find the refractive index that lies in the range of 10 GHz to a few THz,[46] and it is also used to determine the dielectric properties of coordination polymer materials.[47] The absorption coefficients of the H_2BDC ligand and Cd-MOF in the frequency range of 0.1−2.78 THz are presented in Figure 2c. Spectra of both samples show peaks at 1.41 THz (46.88 cm^{-1}). The peak at 2.07 THz (69.35 cm^{-1}) in H_2BDC is slightly shifted to a lower frequency of 2.05 THz (68.37 cm^{-1}) in Cd-MOF. H_2BDC shows a peak at 2.49 THz (83.02 cm^{-1}), while in Cd-MOF, a shoulder is observed at this position. Cd-MOF shows absorption at 2.25 THz (75.21 cm^{-1}), which is not present in H_2BDC. The presence of these absorption bands is in accordance with the calculated spectra of Zn-MOF-5.[48,49] The presence of absorptions at 1.41, 2.07, and 2.49 THz in both Cd-MOF and the H_2BDC linker suggests that these absorptions are associated with the collective motions of the linker molecules. This fact is also supported by Schrock et al.[48] The absorption peak at 2.25 THz in Cd-MOF may be due to Cd clusters, as was also suggested by Nina et al[50] for Zn-MOF-5. Figure 2d shows the real and imaginary parts of the dielectric constant of Cd-MOF and H_2BDC in the frequency range of 0.1−2.78 THz. The real and imaginary dielectric constants of Cd-MOF are higher than those of H_2BDC for all frequencies, except at higher frequencies for which the imaginary dielectric constant is lower for Cd-MOF. The peaks and humps in the dielectric constant at different frequencies are associated with the vibrational motions, as described above. The higher real dielectric constant of Cd-MOF may be due to its increased crystallinity than that of H_2BDC. Further, heavier atoms (i.e., Cd) have higher electronic polarizability, which supports the higher dielectric constant of Cd-MOF. Similar behavior of the real dielectric constant is also observed for crystalline and amorphous aluminum oxide.[51]

2.5. NLO Properties. Nonlinear optical properties are important for optical devices and the telecommunication industry. Nonlinear optical properties can be affected by molecular planarity, π-electron delocalization, and substituent change associated with the molecule and solvent. The hyperpolarizability value is generally related to the nonlinear optical properties (NLO) for a single molecule or the repeating unit of a coordination polymer. The reported hyperpolarizabilities for second harmonic generation of different cadmium metal−organic frameworks are 0.6 × urea,[52] 0.7 × urea,[53] 1.5 × KDP,[54] 2.3 × KDP,[54] 2 × KDP,[55] and 3 × KDP[55] (KDP, potassium dihydrogen phosphate). Although experimental NLO calculations for any material are very important, but being an option, the NLO potential of the material can be analyzed using theoretical chemistry without applying experimental techniques.[56] Cd-MOF is investigated at the B3LYP/LANL2DZ level in the gas phase. The static dipole moment (μ), average linear polarizability (α), anisotropic polarizability ($\Delta\alpha$), the first hyperpolarizability (β), and optical softness (σ_O) of the cadmium compound and urea were calculated and compared, as given in Table 1. The static dipole moment, average linear polarizability, anisotropic polarizability, the first hyperpolarizability, and optical softness are calculated to be 1.916 D, 2.197 Å^3, 9.659 Å^3, 4.232 × 10^{-28} cm^5 esu^{-1}, and 0.120 eV^{-1}, respectively, for urea, and 3.143 D, 108.353 Å^3, 272.224 Å^3, 1.614 × 10^{-26} cm^5 esu^{-1}, and 4.407 eV^{-1} for the cadmium MOF, respectively. According to these results, the NLO properties of Cd-MOF are better than those of urea.

Table 1. Nonlinear Optical Parameters for Cd-MOF and Urea

NLO parameters	Cd-MOF	Urea
static dipole moment (μ) [D]	3.143	1.916
average linear polarizability (α) [Å^3]	108.353	2.197
anisotropic polarizability ($\Delta\alpha$) [Å^3]	272.224	9.659
first hyperpolarizability (β) [cm^5 esu^{-1}]	1.614 × 10^{-26}	4.232 × 10^{-28}
optical softness (σ_O) [eV^{-1}]	4.407	0.120

2.6. Powder XRD of $(C_8H_{10}CdO_7)_n{\cdot}4H_2O$, PC900, and Pt-Ni@PC900. The phase purity of the $(C_8H_{10}CdO_7)_n{\cdot}4H_2O$ crystals was confirmed by the mutual resemblance between the single-crystal data obtained from the simulation and the experimental powder XRD patterns presented in Figure 3a. The powder XRD patterns of PC900 and Pt-Ni@PC900 are presented in Figure 3b. The absence of any peak for CdO in PC900 confirms the elimination and evaporation of the Cd metal with reference to the PDF card number 65-2908.[57] The framework first decomposed into a CdO composite; then, under argon supply, CdO was reduced to the Cd metal, which evaporated upon heating up to 900 °C, as the boiling point of Cd is 767 °C, leaving behind the porous carbon material. The broad peaks present in the PXRD of PC900 at 2θ values near about 22.5 and 43.6° are the characteristic peaks related to the 002 and 100 planes of the carbon material. The PXRD of the Pt-Ni@PC900 composite exhibited peaks at 2θ values of 39.9° (111), 46.4° (200), 67.7° (220), and 81.6° (311) related to Pt. The 2θ peak positions for pure Pt are 39.4, 45.96, 67.36, and 81.01°, which are at lower 2θ values than those reported here for the Pt-Ni@PC900 composite and may be related to the modification in the lattice constants of Pt and Ni metals.[58−60] The information collected from the high-intensity peak at a 2θ value of 39.8° (111) are the interplanar spacing (d111, 0.226 nm), lattice parameter (α, 0.392 nm), full-width at half-maximum (FWHM, 0.0180 radian), and crystallite size (Dcryst, 8.19 nm).

2.7. XPS Analysis of PC900 and Pt-Ni@PC900. The curve-fit spectra of C 1s related to PC900 were deconvoluted into four peaks, C═O (285.96 eV), C−C (285.1 eV), C−O (284.6 eV), and C═C (284.1 eV), as shown in Figure 3c.[61,62] The C 1s spectra related to Pt-Ni@PC900 were resolved into four peaks resulting at C═O (285.7 eV), C−C (285 eV), C−O (284.7), and C═C (284.2), as shown in Figure 3c. The platinum metal doublets related to Pt-Ni@PC900 appear at two different positions of binding energies, as shown in Figure 3d; the doublet peak with a higher binding energy is related to Pt $4f_{5/2}$, and the other band at a lower binding energy is related to Pt $4f_{7/2}$. The deconvolution of the doublet resulted in five peaks. The high-intensity bands present at binding energies of

DOI: 10.1021/acsomega.9b02741
ACS Omega 2020, 5, 2123−2132

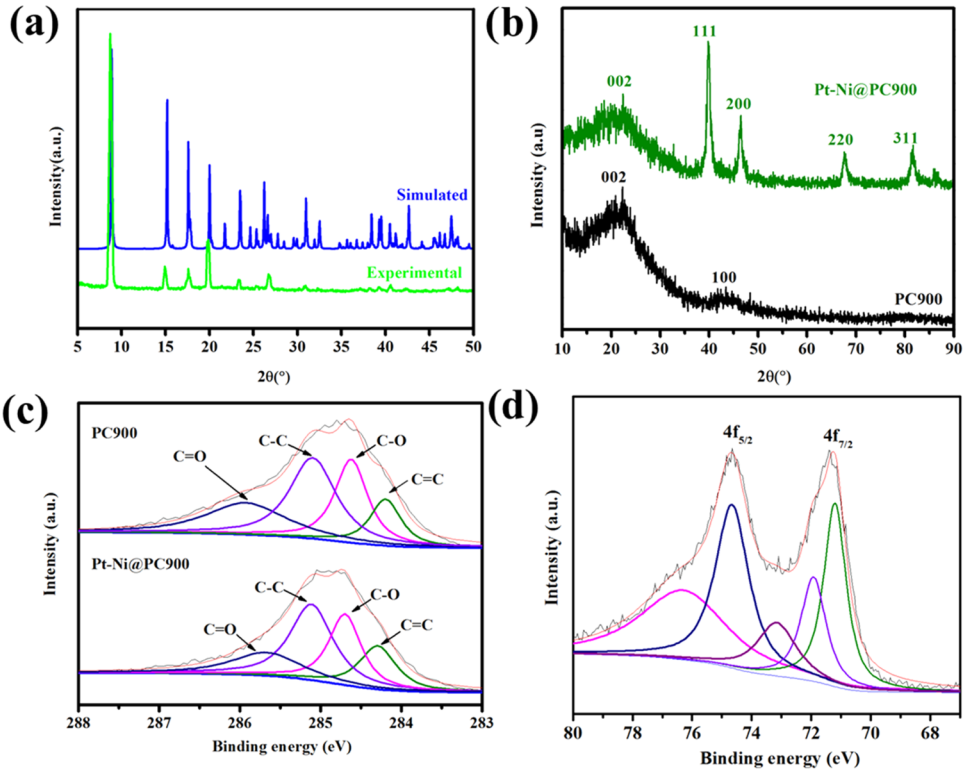

Figure 3. (a) Simulated and experimental powder XRD patterns of $[C_8H_{10}CdO_7]_n{\cdot}4H_2O$. (b) Powder XRD patterns of PC900 and Pt-Ni@PC900. (c) C 1s core-level XPS spectra of PC900 and Pt-Ni@PC900. (d) Pt 4f core-level XPS spectra of Pt-Ni@PC900.

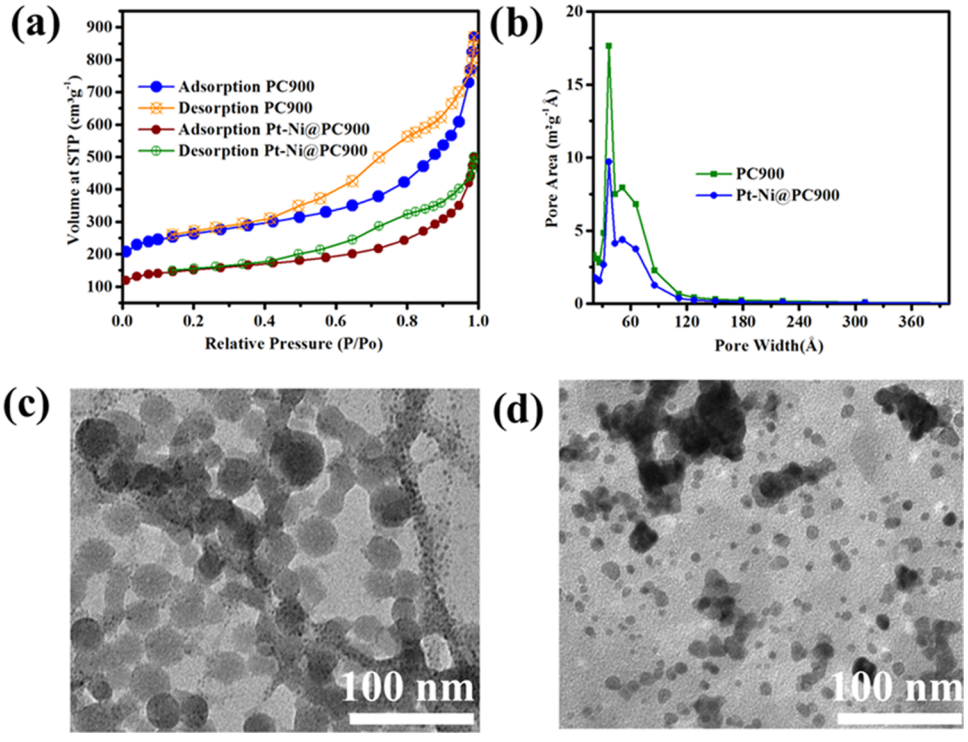

Figure 4. (a) N_2 sorption isotherm at 77 K and (b) pore size distribution plot of PC900 and Pt-Ni@PC900. TEM images of (c) PC900 and (d) Pt-Ni@PC900.

71.2 and 74.6 eV are related to metallic Pt. The small-intensity peaks at 72.0, 73.2 and 76.3 eV are due to the oxides of Pt. The negative shift of 0.4 eV in comparison with the standard binding of Pt (71.8 eV)[63] provides information that the Pt metal is involved in the electron donation and acceptance process with the second metal, which is Ni, an indication of the existence of a core−shell structure.[64] The Ni 2p XPS spectrum of Pt-Ni@PC900 contains core peaks related to Ni $2p_{3/2}$ and $2p_{1/2}$, which is further resolved into four peaks shown in Figure S3a. The metallic Ni peaks are at 854.8 and 873.6 eV, while the

DOI: 10.1021/acsomega.9b02741
ACS Omega 2020, 5, 2123−2132

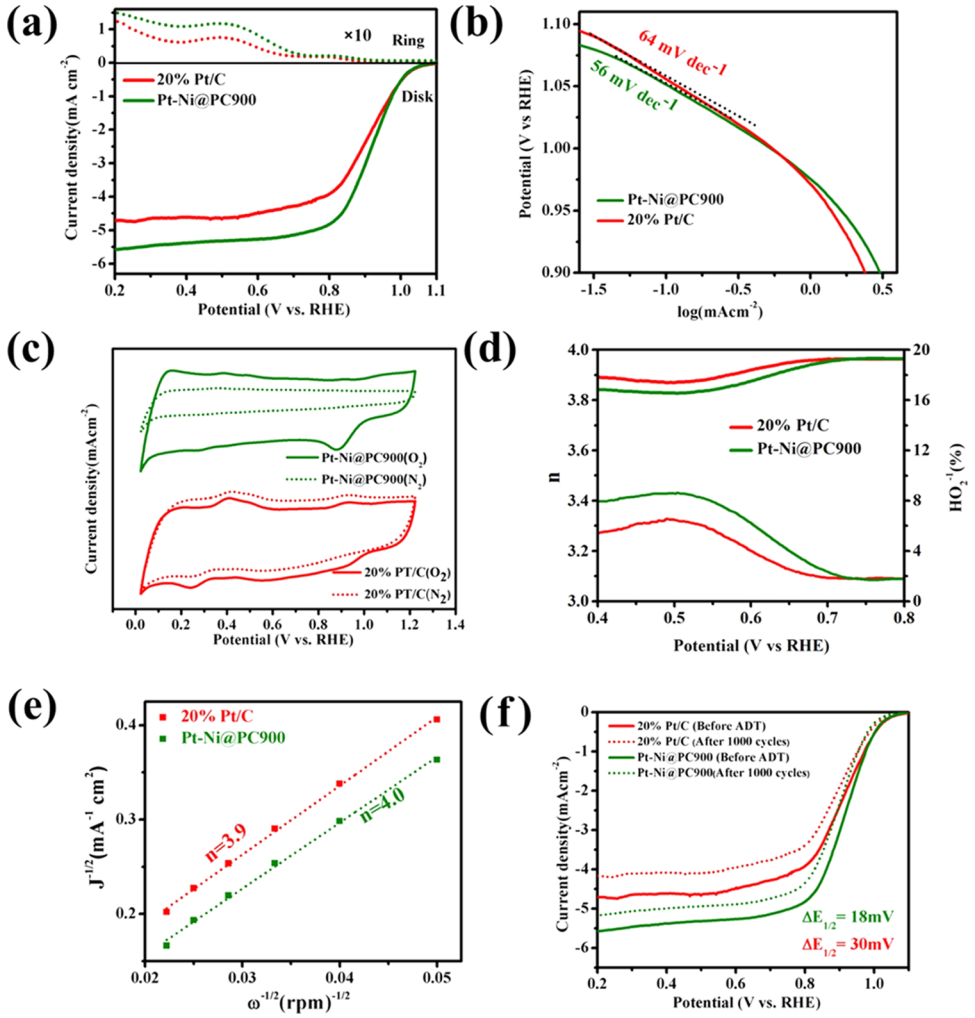

Figure 5. (a) ORR results for Pt-Ni@PC900 and 20% Pt/C at a rotation rate of 1600 rpm in the basic electrolyte of 0.1 M KOH with oxygen saturation at 5 mV s^{-1} through a constant potential of 1.5 volt vs RHE applied on the Pt-ring; the disk current is located at the lower side, while the ring current, called the positive current, is present on the upper side (dotted curves). (b) Tafel plots from ORR LSV results (at 1600 rpm) for Pt-Ni@PC900 and 20% Pt/C. (c) CV curves of Pt-Ni@PC900 and 20% Pt/C on the RDE with 50 mV/s scan rate under saturated nitrogen (dotted lines) and O_2 (solid lines) in 0.1 M KOH. Pt-Ni@PC900 shows much more positive ORR onset potential and higher cathodic current than 20% Pt/C. (d) Electron number and H_2O_2 yield results gathered from RRDE data displayed at different potentials vs RHE. (e) K-L plots for Pt-Ni@PC900 and 20% Pt/C at 0.7 V vs RHE. (f) LSV results for Pt-Ni@PC900 and 20% Pt/C before and after ADTs.

nickel oxide peaks are at 861.8 and 879.7 eV.[65] The Ni peak of Pt-Ni@PC900 shows a positive deviation with reference to the standard nickel metal peak at 852.6 eV. The O 1s core line of Pt-Ni@PC900 (Figure S3b) is a convolution of two broad peaks at 531.9 eV for (M-O) and 533.3 eV for (C-O).[66] The elemental analysis by XPS, CHNS/O, and metal composition confirmed by ICP is presented in Table S4. The percentage atomic composition of Pt-Ni@PC900 found from XPS is Pt 4f (5.8%), Ni 2p (2.92%), C 1s (80.94%), and O 1s (10.34%). The ICP results show Pt to be 6.03% and Ni to be 3.73% for Pt-Ni@PC900. The percentage of elements from ICP is slightly higher than that found from XPS. The CHNS/O results correlate with theoretical calculations and also show better agreement with XPS results.

2.8. Raman Spectroscopy of PC900 and Pt-Ni@PC900. The chemistry of PC900 and Pt-Ni@PC900 can be further understood through Raman spectroscopy. The Raman spectra of PC900 and Pt-Ni@PC900 are shown in Figure S4. The PC900 spectrum shows two peaks, one at ∼1584 cm^{-1} with an intensity of 21.2 called the G-band is the characteristic identity of the graphitic layer that appears due to E_{2g} phonon of the sp^2 carbon atoms. The other peak located at ∼1339 cm^{-1} with an intensity of 22.3 corresponds to the D-band, which can be assigned to the A_{1g} mode breathing vibrations of the aromatic rings that are bound to sp^3-C at the edges and defect sites. The ratio of the intensities of the D- and G-bands ($R = I_D/I_G$) informs about the range of structurally ordered graphite sites present in the porous carbon material. The intensity of the D-band is higher in PC900 and the Pt-Ni@PC900 composite than that of the G-band owing to the presence of disordered and defects sites in all compounds. The positions of the D- and G-bands along with their intensities and intensity ratio for all compounds are given in Table S5.

2.9. Nitrogen Adsorption Analysis. The specific surface area, pore volume, and pore-size distribution were obtained for $[C_8H_{10}CdO_7]_n{\cdot}4H_2O$, porous carbon (PC900) and Pt-Ni@PC900 through N_2 adsorption−desorption measurements. The details of all aforementioned parameters are given in Table S6. The isotherms and pore volume distribution curves for PC900 and Pt-Ni@PC900 are presented in Figure 4a,b. All isotherms

DOI: 10.1021/acsomega.9b02741
ACS Omega 2020, 5, 2123−2132

showed type IV characteristics with an H_3 hysteresis loop.[67] The BET surface area of PC900 obtained by heating Cd-MOF in an inert atmosphere was calculated to be 877 $m^2 g^{-1}$. It is a well-known fact that for an electrochemical reduction process a carbon substrate with a high surface area is very much important to prepare composites for electrocatalytic activity due to the fact that there is an increase in the diffusion rate and mass transfer of the electrolyte. The total pore volume of pores with less than 73.03 nm width for PC900 at P/P_o = 0.97 was found to be 1.128934 $cm^3 g^{-1}$. The BET adsorption average pore width was 5.1 nm for PC900. The large surface area of PC900 was the main reason for selecting this material as a substrate to synthesize bimetallic hybrids. A prominent decrease in BET surface area and total pore volume was observed for the prepared bimetallic composites. The BET surface area and total pore volume of Pt-Ni@PC900 were calculated to be 359.49 $m^2 g^{-1}$ and 0.43 $cm^3 g^{-1}$, respectively. The isotherm of Pt-Ni@PC900 was similar to that of its carbon substrate PC900. The decrease in the surface area and pore volume was related to the loading of metal nanoparticles, especially for the microporous region.[68] The intense peak found at 3.8 nm for PC900 near the microporous region showed the formation of the mesoporous carbon material by the evaporation of Cd. The intensity of the peak situated at 3.8 nm for Pt-Ni@PC900 was decreased. The reduction in the intensity was related to the fact that not all but most of the pores were filled with metal particles.

2.10. Surface Morphology. SEM images related to Cd-MOF, PC900, and Pt-Ni@PC900 are presented in Figure S5a−c, respectively. In the pristine framework, $(C_8H_{10}CdO_7)_n \cdot 4H_2O$, there are sheets with average dimensions of 370 × 162 μm, as shown in Figure S5a. These sheets were cracked upon heating up to 900 °C due to elimination of the cadmium metal, being volatile at 767 °C in an argon atmosphere. The cracked broken sheets with average dimensions 150 × 99 μm related to the PC900 carbon material can be seen in Figure S5b. The sheets with average dimensions 33 × 54 μm related to the catalytic material, Pt-Ni@PC900, are presented in Figure S5c. The surface of Pt-Ni@PC900 appears to be smooth in some areas of the sheet due to the filling of cracks with metal particles, while there are still some cracks that might support the catalytic process.

TEM images for PC900 and Pt-Ni@PC900 are shown in Figure 4c,d, respectively. Nanostructured PC900 with a spherical morphology has an average particle size of ∼23 nm. The dense spots with an average particle size of ∼3.9 nm for Pt-Ni@PC900 indicate the presence of metal nanoparticles supported on the carbon material.

2.11. Oxygen Reduction Reaction. The oxygen reduction reaction was carried out by utilizing a rotating ring disk electrode (RRDE) at 1600 rpm with a scan rate of 5 mV s^{-1} in 0.1 M KOH solution as the electrolyte with oxygen saturation. ORR polarization curves of Pt-Ni@PC900 and 20% Pt/C are presented in Figure 5a. The onset potential (potential at 1% of the total limiting current density) for Pt-Ni@PC900 and 20% Pt/C are 1.067 and 1.079 V, respectively. The onset potential related to Pt-Ni@PC900 is 25 mV more negative than that of 20% Pt/C. The half-wave potentials of Pt-Ni@PC900 and 20% Pt/C are 0.909 and 0.90 V vs RHE. The half-wave potential of Pt-Ni@PC900 is relatively more positive than that of 20% Pt/C. The half-wave potential and limiting current density of Pt-Ni@PC900 are comparatively better than those of the commercial 20% Pt/C catalyst. Therefore, it can be easily concluded that Pt-Ni@PC900 is the best ORR catalyst. The ORR activity is also verified by the Tafel slope; the smaller slope is related to better ORR activity. The Tafel slope (Figure 5b) found for Pt-Ni@PC900 is 56 mV $decade^{-1}$, which is less than 64 mV $decade^{-1}$ (20% Pt/C). CV of Pt-Ni@PC900 and 20% Pt/C was performed in 0.1 M KOH solution using a ring disk electrode under saturated N_2 and O_2 at a scan rate of 50 mV s^{-1} (Figure 5c). CV curves under O_2 presented a prominent ORR peak (solid line), while the corresponding peak was absent in the CV curve under N_2 (dashed line).

The number of electrons transferred (n) for one O_2 molecule and HO_2^{-1} yield (which is the reaction intermediate) decide whether the ORR process is by two electrons or four electrons. Both (n) and HO_2^{-1} yield are shown in Figure 5d. The HO_2^{-1} yield is found to be less than 8% for Pt-Ni@PC900, which is comparable to that of 20% Pt/C, for which the HO_2^{-1} yield is less than 7%. This is an indication of the best ORR performance of Pt-Ni@PC900 with 7% Pt. The n values lie between 3.84 and 3.91, suggesting that the ORR catalyzed by all catalysts proceeds mainly via a four-electron process ($O_2 + 2H_2O + 4e^{-1} \rightarrow 4OH^{-1}$). The two-electron process ($O_2 + H_2O + 2e^{-1} \rightarrow OH^{-1} + HO_2^{-1}$) is less feasible compared to the four-electron process for all electrocatalysts.

Koutecky−Levich plots (J^{-1} vs $\omega^{-1/2}$) obtained from LSV curves at different rotation speeds and 0.7 V vs RHE for Pt-Ni@PC900 and 20% Pt/C are presented in Figure 5e. The graph shows good linear fitting for the first-order kinetics, and the calculated number of electrons supports the four-electron process for all catalysts in this study. The kinetic current density calculated at 0.7 V vs RHE for Pt-Ni@PC900 and 20% Pt/C is 58 and 29 mA cm^{-2}, respectively.

LSV on an RDE with different rotation speeds from 400 to 2025 rpm was done to correlate the ORR process with the RRDE analysis by fixing similar electrochemical parameters to those used during ORR measurements with the RRDE. LSV results at different rotation speeds for Pt-Ni@PC900 and 20% Pt/C are shown in Figure S6a,b, respectively. The limiting current density increases with the increase of rotation speed.

Accelerating durability tests (ADTs) were performed for our synthesized catalysts and commercial 20% Pt/C to check their practical usability in fuel cells. The ADTs for all catalysts in this study were carried out in O_2-saturated 0.1 M KOH electrolyte for 1000 cycles at a scan rate of 50 mV s^{-1} using an RDE at 25 °C. The O_2 flow remained continuous throughout 1000 cycles. After the completion of 1000 cycles, CV and LSV were performed. It was found through CV that the loss of electrochemical active surface area for Pt-Ni@PC900 and 20% Pt/C was 18 and 35%, respectively, as shown in Figure S7. LSV curves taken at 1600 rpm after 1000 CV cycles are presented in Figure 5f. LSV results after ADT showed that the difference in both the onset and half-wave potentials for Pt-Ni@PC900 is 19 mV after 1000 CV cycles, whereas 20% Pt/C shows a difference of 17 mV for the onset and 30 mV for the half-wave potential. The stability and durability of our synthesized catalysts are enhanced. These curves are coherent with the CV findings for all catalysts. The results of ADTs (Table 2) clearly demonstrate that the synthesized catalyst, Pt-Ni@PC900, shows excellent stability and durability compared with the commercially available 20% Pt/C catalyst. The working electrode stability test for Pt-Ni@PC900 was run in 1 M KOH alkaline solution, as shown in Figure S8. The hybrid retained a constant current density (67 mA cm^{-2}) under a

DOI: 10.1021/acsomega.9b02741
ACS Omega 2020, 5, 2123−2132

Table 2. Electrochemical Parameters and Tafel Slope Results for 20% PT/C and Pt-Ni@PC900

compounds	20% PT/C	Pt-Ni@PC900
onset (V vs RHE), before ADT	1.079	1.067
onset (V), after ADT	1.062	1.048
$E_{1/2}$ (V), before ADT	0.90	0.91
$E_{1/2}$ (V), after ADT	0.87	0.89
limiting current density (mA cm^{-2}), before ADT	−4.72	−5.58
limiting current density (mA cm^{-2}), after ADT	−4.21	−5.14
Tafel slope (mV dec^{-1})	64	56

constant potential of 0.5 V for 12 h, which is good sign of durability and stability.

3. CONCLUSIONS

Cd-MOF with empirical formula $[C_8H_{10}CdO_7]_n{\cdot}4H_2O$ was synthesized, characterized, and theoretically verified by various analytical techniques. The framework was also analyzed by THz-TD spectroscopy to calculate collective vibrations of the coordination polymer at low frequencies that was helpful to characterize the polymer relative to the linker. THz-TD spectroscopy showed a higher value of the real dielectric constant for Cd-MOF as compared to H_2BDC, which was due to the increased electronic polarizability by the incorporation of the heavier Cd metal atom and also owing to the increased crystallinity compared to H_2BDC. Nonlinear optical analysis through DFT showed that the first static hyperpolarizability of Cd-MOF was 38 times higher than that of NLO-active urea. Nanostructured carbon with a high surface area obtained through carbonization of Cd-MOF was used as a support for the preparation of Pt-Ni@PC900. ORR measurements performed using Pt-Ni@PC900 with 7% Pt as the working electrode material showed excellent performance in terms of efficiency and durability over the commercially available 20% Pt/C catalyst.

4. EXPERIMENTAL SECTION

The computational method, characterization techniques, and ORR measurement details are described in the Supporting Information.

4.1. Synthesis of $[C_8H_{10}CdO_7]_n{\cdot}4H_2O$. A mixture of 1,4-benzenedicarboxylic acid (150 mg, 0.9 mmol) and cadmium acetate dehydrate (240.65 mg, 0.9 mmol) along with potassium hydroxide (101 mg, 1.8 mmol) in 40 mL of deionized water was sonicated for 2 h in a 100 mL Teflon vial. The homogeneous mixture was then sealed in a 100 mL steel autoclave. The autoclave was heated up to 160 °C for 72 h and then cooled at a rate of 5 °C/min. Good-quality colorless needlelike crystals were obtained with a yield of 74%.

4.2. Carbonization of $[C_8H_{10}CdO_7]_n{\cdot}4H_2O$. Cd-MOF was sacrificed through heat treatment by placing 2 g of it in a tube furnace coupled with argon gas supply. The temperature of the furnace was raised up to 900 °C in three steps, i.e., the temperature was kept constant for 1 h at 400 °C, then for 1 h at 600 °C, and in the end for 4 h at 900 °C. The obtained black color crystalline material was cooled, dried, and named PC900.

4.3. Synthesis of Pt-Ni@PC900. The Pt-Ni@PC900 composite was prepared according to the polyol reduction method; 120 mg of PC900 was dispersed in ethylene glycol solvent through a sonication process for 1 h. The homogenized dispersed suspension was then heated up to 100 °C, and the temperature of the mixture was kept constant, i.e., at 100 °C, during dropwise slow addition of two separate salt solutions, i.e., 10 mL of an aqueous solution of $Ni(CH_3COOH)_2{\cdot}4H_2O$ and 10 mL of an aqueous solution of $H_2PtCl_6{\cdot}6H_2O$. The suspension was then refluxed for 5 h, which resulted in the formation of a composite with a Pt:Ni weight ratio of 7:5. The synthesis of $[C_8H_{10}CdO_7]_n{\cdot}4H_2O$ and Pt-Ni@PC900 is presented in Scheme 1.

■ ASSOCIATED CONTENT

Supporting Information

The Supporting Information is available free of charge at https://pubs.acs.org/doi/10.1021/acsomega.9b02741.

Molecular orbital energy diagram; Contour diagram of molecular orbitals and MEP map of Cd-MOF; XPS spectra of Ni and O related to Pt-Ni@PC900; Raman spectra of PC900 and Pt-Ni@PC900; SEM images of Cd-MOF, PC900, and Pt-Ni@PC900; RDE graphs and ADT CV curves of Pt-Ni@PC900 and 20% Pt/C; Durability test of Pt-Ni@PC900 (PDF)

■ AUTHOR INFORMATION

Corresponding Author

*E-mail moazzamhussain_b@yahoo.com. Phone: 0092519057262.

ORCID

Muhammad Nadeem: 0000-0002-3764-1384
Ghulam Yasin: 0000-0001-8794-3965
Moazzam H. Bhatti: 0000-0003-4868-6032
Koray Sayin: 0000-0001-6648-5010

Author Contributions

#M.N. and G.Y. contributed equally to this paper.

Notes

The authors declare no competing financial interest.

■ ACKNOWLEDGMENTS

The authors thank Allama Iqbal Open University, Islamabad, Pakistan Institute of Engineering and Applied Sciences, Islamabad, National Institute of Laser and Optics, Islamabad, and Beijing University of Chemical Technology, China, for characterization and experimental facilities. Muhammad

Scheme 1. Scheme of the Synthesis of $[C_8H_{10}CdO_7]_n{\cdot}4H_2O$ and Pt-Ni@PC900

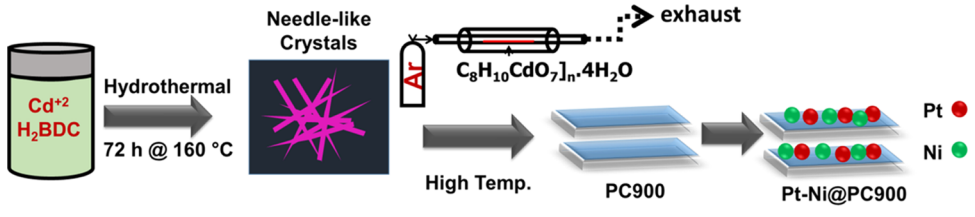

DOI: 10.1021/acsomega.9b02741
ACS Omega 2020, 5, 2123−2132

Nadeem acknowledges the IRSIP scholarship (PIN: 34 PSc 30) provided by the Higher Education Commission (HEC) of Pakistan for financial support while carrying out the research work in Beijing University of Chemical Technology, China.

REFERENCES

(1) Miller, E. Photoelectrochemical water splitting. *Energy Environ. Sci.* **2015**, *8*, 2809−2810.
(2) Majeed, A.; Hou, P. X.; Zhang, F.; Tabassum, H.; Li, X.; Li, G. X.; Liu, C.; Cheng, H. M. A Freestanding Single-Wall Carbon Nanotube Film Decorated with N-Doped Carbon-Encapsulated Ni Nanoparticles as a Bifunctional Electrocatalyst for Overall Water Splitting. *Adv. Sci.* **2019**, No. 1802177.
(3) Qiu, T.; Liang, Z.; Guo, W.; Gao, S.; Qu, C.; Tabassum, H.; Zhang, H.; Zhu, B.; Zou, R.; Shao-Horn, Y. Highly exposed ruthenium-based electrocatalysts from bimetallic metal-organic frameworks for overall water splitting. *Nano Energy* **2019**, *58*, 1−10.
(4) Bing, Y.; Liu, H.; Zhang, L.; Ghosh, D.; Zhang, J. Nanostructured Pt-alloy electrocatalysts for PEM fuel cell oxygen reduction reaction. *Chem. Soc. Rev.* **2010**, *39*, 2184−2202.
(5) Zhang, J. *PEM Fuel Cell Electrocatalysts and Catalyst Layers: Fundamentals and Applications*; Springer Science & Business Media, 2008.
(6) Gewirth, A. A.; Thorum, M. S. Electroreduction of dioxygen for fuel-cell applications: materials and challenges. *Inorg. Chem.* **2010**, *49*, 3557−3566.
(7) Pan, L.; Ott, S.; Dionigi, F.; Strasser, P. Current challenges related to the deployment of shape controlled Pt alloy ORR nanocatalysts into low-Pt loaded cathode layers of Proton Exchange Membrane Fuel Cells (PEMFC). *Curr. Opin. Biotechnol. Electrochem.* **2019**, 61.
(8) Ren, X.; Lv, Q.; Liu, L.; Liu, B.; Wang, Y.; Liu, A.; Wu, G. Current progress of Pt and Pt-based electrocatalysts used for fuel cells *Sustainable Energy Fuels* 2020, DOI: 10.1039/C9SE00460B.
(9) Tian, X.; Zhao, X.; Su, Y.-Q.; Wang, L.; Wang, H.; Dang, D.; Chi, B.; Liu, H.; Hensen, E. J.; Lou, X. W. D.; et al. Engineering bunched Pt-Ni alloy nanocages for efficient oxygen reduction in practical fuel cells. *Science* **2019**, *366*, 850−856.
(10) Nale, A.; Negro, E.; Bang, Y.; Vezzù, K.; Pagot, G.; Pace, G.; Polizzi, S.; Bertoncello, R.; Di Noto, V. In Interplay between Activation Processes, Physicochemical Properties and Electrochemical Performance of "Core-Shell" Carbon Nitride Pt-Ni ORR Electrocatalysts Based on Hierarchical Graphene Supports, Meeting Abstracts. *Electrochem. Soc.* **2019**, 759.
(11) Reyes-Rodríguez, J. L.; Velázquez-Osorio, A.; Bahena-Uribe, D.; Soto-Guzmán, A.; Leyva, M.; Rodríguez-Castellanos, A.; Citalán-Cigarroa, S.; Solorza-Feria, O. Tailoring the morphology of Ni−Pt nanocatalysts through the variation of oleylamine and oleic acid: a study on oxygen reduction from synthesis to fuel cell application. *Catal. Sci. Technol.* **2019**, *9*, 2630−2650.
(12) Khodakov, A.; Olthof, B.; Bell, A. T.; Iglesia, E. Structure and catalytic properties of supported vanadium oxides: support effects on oxidative dehydrogenation reactions. *J. Catal.* **1999**, *181*, 205−216.
(13) Yang, H.; Zou, H.; Chen, M.; Li, S.; Jin, J.; Ma, J. The green synthesis of ultrafine palladium−phosphorus alloyed nanoparticles anchored on polydopamine functionalized graphene used as an excellent electrocatalyst for ethanol oxidation. *Inorg. Chem. Front.* **2017**, *4*, 1881−1887.
(14) Yang, L.; Shui, J.; Du, L.; Shao, Y.; Liu, J.; Dai, L.; Hu, Z. Carbon-Based Metal-Free ORR Electrocatalysts for Fuel Cells: Past, Present, and Future. *Adv. Mater.* **2019**, *31*, No. 1804799.
(15) Garapati, M. S.; Sundara, R. Highly efficient and ORR active platinum-scandium alloy-partially exfoliated carbon nanotubes electrocatalyst for Proton Exchange Membrane Fuel Cell. *Int. J. Hydrogen Energy* **2019**, *44*, 10951−10963.
(16) Martins, M.; Metin, Ö.; Šljukić, B.; Sevim, M.; Sequeira, C.; Santos, D. PdNi alloy nanoparticles assembled on cobalt ferrite-carbon black composite as a fuel cell catalyst. *Int. J. Hydrogen Energy* **2019**, *44*, 14193−14200.
(17) Sharma, S.; Zeng, C.; Peterson, A. A. Face-centered tetragonal (FCT) Fe and Co alloys of Pt as catalysts for the oxygen reduction reaction (ORR): A DFT study. *J. Chem. Phys.* **2019**, *150*, No. 041704.
(18) He, T.; Chen, R.; Lim, Z. B.; Rajwar, D.; Ma, L.; Wang, Y.; Gao, Y.; Grimsdale, A. C.; Sun, H. Efficient Energy Transfer under Two-Photon Excitation in a 3D, Supramolecular, Zn (II)-Coordinated, Self-Assembled Organic Network. *Adv. Opt. Mater.* **2014**, *2*, 40−47.
(19) Cui, Y.; Li, B.; He, H.; Zhou, W.; Chen, B.; Qian, G. Metal−organic frameworks as platforms for functional materials. *Acc. Chem. Res.* **2016**, *49*, 483−493.
(20) Kaskel, S. *The Chemistry of Metal-Organic Frameworks: Synthesis, Characterization, and Applications*; John Wiley & Sons, 2016; Vol. *1*.
(21) Medishetty, R.; Zaręba, J. K.; Mayer, D.; Samoć, M.; Fischer, R. A. Nonlinear optical properties, upconversion and lasing in metal−organic frameworks. *Chem. Soc. Rev.* **2017**, *46*, 4976−5004.
(22) Chen, Y.-Z.; Cai, G.; Wang, Y.; Xu, Q.; Yu, S.-H.; Jiang, H.-L. Palladium nanoparticles stabilized with N-doped porous carbons derived from metal−organic frameworks for selective catalysis in biofuel upgrade: the role of catalyst wettability. *Green Chem.* **2016**, *18*, 1212−1217.
(23) Lu, J.; Zhou, W.; Wang, L.; Jia, J.; Ke, Y.; Yang, L.; Zhou, K.; Liu, X.; Tang, Z.; Li, L.; et al. Core−shell nanocomposites based on gold nanoparticle@ zinc−iron-embedded porous carbons derived from metal−organic frameworks as efficient dual catalysts for oxygen reduction and hydrogen evolution reactions. *ACS Catal.* **2016**, *6*, 1045−1053.
(24) Sun, J. K.; Xu, Q. Metal nanoparticles immobilized on carbon nanodots as highly active catalysts for hydrogen generation from hydrazine in aqueous solution. *ChemCatChem* **2015**, *7*, 526−531.
(25) Xia, B.; Chen, K.; Luo, W.; Cheng, G. NiRh nanoparticles supported on nitrogen-doped porous carbon as highly efficient catalysts for dehydrogenation of hydrazine in alkaline solution. *Nano Res.* **2015**, *8*, 3472−3479.
(26) Feng, C.; Hao, Y.; Zhang, L.; Shang, N.; Gao, S.; Wang, Z.; Wang, C. AgPd nanoparticles supported on zeolitic imidazolate framework derived N-doped porous carbon as an efficient catalyst for formic acid dehydrogenation. *RSC Adv.* **2015**, *5*, 39878−39883.
(27) Fu, S.; Song, J.; Zhu, C.; Du, D.; Lin, Y. Metal-Organic Frameworks Based Porous Carbons for Oxygen Reduction Reaction Electrocatalysts for Fuel Cell Applications. *Nanocarbon Electrochem.* **2019**, 251.
(28) Yang, H.; Zhang, X.; Zou, H.; Yu, Z.; Li, S.; Sun, J.; Chen, S.; Jin, J.; Ma, J. Palladium nanoparticles anchored on three-dimensional nitrogen-doped carbon nanotubes as a robust electrocatalyst for ethanol oxidation. *ACS Sustainable Chem. Eng.* **2018**, *6*, 7918−7923.
(29) Yang, L.-M.; Ravindran, P.; Vajeeston, P.; Svelle, S.; Tilset, M. A quantum mechanically guided view of Cd-MOF-5 from formation energy, chemical bonding, electronic structure, and optical properties. *Microporous Mesoporous Mater.* **2013**, *175*, 50−58.
(30) Zhang, F.; Bei, F.-L.; Cao, J.-M. Sovolthermal Synthesis and Crystal Structure of Two Cd II Coordination Polymers of Benzenedicarboxylic. *J. Chem. Crystallogr.* **2008**, *38*, 561−565.
(31) Zhang, F.; Bei, F.-L.; Cao, J.-M.; Wang, X. The preparation of CdO nanowires from solid-state transformation of a layered metal-organic framework. *J. Solid State Chem.* **2008**, *181*, 143−149.
(32) Zhang, F.; Bei, F.-L.; Cao, J.-M. Sovolthermal Synthesis and Crystal Structure of Two Cd II Coordination Polymers of Benzenedicarboxylic. *J. Chem. Crystallogr.* **2008**, *38*, 561−565.
(33) Zhang, F.; Bei, F.-L.; Cao, J.-M.; Wang, X. The preparation of CdO nanowires from solid-state transformation of a layered metal-organic framework. *J. Solid State Chem.* **2008**, *181*, 143−149.
(34) Uçar, İ.; Yeşilel, O. Z.; Bulut, A.; Içbudak, H.; Ölmez, H.; Kazak, C. A capped trigonal prismatic cadmium complex with tetra- and tridentate ligands: bis (triethanolamine)-κ3N, O, O′; κ4N, O, O′, O″-cadmium (II) squarate monohydrate. *Acta Crystallogr., Sect. C: Cryst. Struct. Commun.* **2004**, *60*, m392−m394.

DOI: 10.1021/acsomega.9b02741
ACS Omega 2020, 5, 2123−2132

(35) Chakraborty, J.; Samanta, B.; Pilet, G.; Mitra, S. Tris (μ-phenoxo) bridged Cd (II) polymer synthesised from a symmetrical tripodal ligand: A novel observation for heptadentate monocapped trigonal antiprismatic Schiff base complex. *Inorg. Chem. Commun.* **2007**, *10*, 40−44.
(36) Vural, H.; Uçar, İ. A combined theoretical and experimental study of chelidamate cadmium (II) complex,[Cd 2 (dpa) 2 (chel) 2]· 2 [Cd (dpa)(chel)]· 6H 2 O. *Spectrochim. Acta, Part A* **2015**, *136*, 1298−1307.
(37) Nakamoto, K. *Infrared and Raman Spectra of Inorganic and Coordination Compounds*; Wiley Online Library, 1986.
(38) Kumar, G.; Srivastava, M. Spectral and magnetochemical studies of nickel (II) and cobalt (II) complexes of hippuric acid. *Rev. Chim. Miner.* **1979**, *16*, 14−8.
(39) Tamer, Ö.; Sarıboğa, B.; Uçar, İ. A combined crystallographic, spectroscopic, antimicrobial, and computational study of novel dipicolinate copper (II) complex with 2-(2-hydroxyethyl) pyridine. *Struct. Chem.* **2012**, *23*, 659−670.
(40) Uçar, İ.; Tamer, Ö.; Sarıboğa, B.; Büyükgüngör, O. Three novel dipicolinate complexes with the pyridine-2, 6-dimethanol−A combined structural, spectroscopic, antimicrobial and computational study. *Solid State Sci.* **2013**, *15*, 7−16.
(41) Tamer, Ö.; Bhatti, M. H.; Yunus, U.; Avcı, D.; Atalay, Y.; Nadeem, M.; Shah, S. R.; Helliwell, M. Structural, spectroscopic, nonlinear optical and electronic properties of calcium N-phthaloyl-glycinate: A combined experimental and theoretical study. *J. Mol. Struct.* **2016**, *1125*, 315−322.
(42) Nadeem, M.; Yunus, U.; Bhatti, M. H.; Ayub, K.; Mehmood, M.; Saif, M. J. Crystal structure, spectroscopic, electronic, luminescent and nonlinear optical properties of (s)-4-Amino-5-(1-hydroxy-ethyl)-2, 4-dihydro-[1, 2, 4] triazole-3-thione: A combined experimental and DFT study. *J. Phys. Chem. Solids* **2017**, *110*, 218.
(43) Ryder, M. R.; Civalleri, B.; Cinque, G.; Tan, J.-C. Discovering connections between terahertz vibrations and elasticity underpinning the collective dynamics of the HKUST-1 metal−organic framework. *CrystEngComm* **2016**, *18*, 4303−4312.
(44) Greaves, G.; Meneau, F.; Majerus, O.; Jones, D.; Taylor, J. Identifying vibrations that destabilize crystals and characterize the glassy state. *Science* **2005**, *308*, 1299−1302.
(45) Schröck, K.; Schröder, F.; Heyden, M.; Fischer, R.; Havenith, M. Characterization of interfacial water in MOF-5 (Zn4(O)(BDC)3)-a combined spectroscopic and theoretical study. *Phys. Chem. Chem. Phys.* **2008**, *10*, 4732−4739.
(46) Duvillaret, L.; Garet, F.; Coutaz, J.-L. Highly precise determination of optical constants and sample thickness in terahertz time-domain spectroscopy. *Appl. Opt.* **1999**, *38*, 409−415.
(47) Jin, Y.-S.; Kim, G.-J.; Jeon, S.-G. Terahertz dielectric properties of polymers. *J. Korean Phys. Soc.* **2006**, *49*, 513−517.
(48) Schröck, K.; Schroder, F.; Heyden, M.; Fischer, R. A.; Havenith, M. Characterization of interfacial water in MOF-5 (Zn4(O)(BDC)3)-a combined spectroscopic and theoretical study. *Phys. Chem. Chem. Phys.* **2008**, *10*, 4732−4739.
(49) Civalleri, B.; Napoli, F.; Noel, Y.; Roetti, C.; Dovesi, R. Ab-initio prediction of materials properties with CRYSTAL: MOF-5 as a case study. *CrystEngComm* **2006**, *8*, 364−371.
(50) Lock, N.; Wu, Y.; Christensen, M.; Cameron, L. J.; Peterson, V. K.; Bridgeman, A. J.; Kepert, C. J.; Iversen, B. B. Elucidating negative thermal expansion in MOF-5. *J. Phys. Chem. C* **2010**, *114*, 16181−16186.
(51) Mehboob, S.; Mehmood, M.; Ahmed, M.; Ahmad, J.; Tanvir, M. T.; Ahmad, I.; ul Hassan, S. M. Terahertz time domain spectroscopy of amorphous and crystalline aluminum oxide nanostructures synthesized by thermal decomposition of AACH. *Mater. Chem. Phys.* **2017**, *191*, 62−69.
(52) Liu, G.-X.; Zhu, K.; Xu, H.-M.; Nishihara, S.; Huang, R.-Y.; Ren, X.-M. Five 3D metal−organic frameworks constructed from V-shaped polycarboxylate acids and flexible imidazole-based ligands. *CrystEngComm* **2010**, *12*, 1175−1185.
(53) Liu, G. X.; Zhu, K.; Chen, H.; Huang, R. Y.; Ren, X. M. New Examples of Metal Coordination Architectures of 3, 3′, 4, 4′-Biphenyltetracarboxylic Acid−Syntheses, Crystal Structures, and Physical Properties. *Z. Anorg. Allg. Chem.* **2009**, *635*, 156−164.
(54) Lin, J.-D.; Wu, S.-T.; Li, Z.-H.; Du, S.-W. Syntheses, topological analyses, and NLO-active properties of new Cd (II)/M (II)(M = Ca, Sr) metal−organic frameworks based on R-isophthalic acids (R = H, OH, and t-Bu). *Dalton Trans.* **2010**, *39*, 10719−10728.
(55) Wang, Y.-T.; Tang, G.-M.; Wei, Y.-Q.; Qin, T.-X.; Li, T.-D.; He, C.; Ling, J.-B.; Long, X.-F.; Weng Ng, S. Two New Nonlinear Optical and Ferroelectric Three-Dimensional Metal− Organic Frameworks with an sqp-net. *Cryst. Growth Des.* **2010**, *10*, 25−28.
(56) Su, X.; Wang, Y.; Yang, Z.; Huang, X.-C.; Pan, S.; Li, F.; Lee, M.-H. Experimental and theoretical studies on the linear and nonlinear optical properties of Bi2ZnOB2O6. *J. Phys. Chem. C* **2013**, *117*, 14149−14157.
(57) Yu, H.; Wang, D.; Han, M.-Y. Top-down solid-phase fabrication of nanoporous cadmium oxide architectures. *J. Am. Chem. Soc.* **2007**, *129*, 2333−2337.
(58) Wang, X.; Vara, M.; Luo, M.; Huang, H.; Ruditskiy, A.; Park, J.; Bao, S.; Liu, J.; Howe, J.; Chi, M.; et al. Pd@ Pt core−shell concave decahedra: a class of catalysts for the oxygen reduction reaction with enhanced activity and durability. *J. Am. Chem. Soc.* **2015**, *137*, 15036−15042.
(59) Sarkar, A.; Manthiram, A. Synthesis of Pt@ Cu core− shell nanoparticles by galvanic displacement of Cu by Pt4+ ions and their application as electrocatalysts for oxygen reduction reaction in fuel cells. *J. Phys. Chem. C* **2010**, *114*, 4725−4732.
(60) Gan, L.; Heggen, M.; Rudi, S.; Strasser, P. Core−Shell Compositional Fine Structures of Dealloyed Pt x Ni1−x Nanoparticles and Their Impact on Oxygen Reduction Catalysis. *Nano Lett.* **2012**, *12*, 5423−5430.
(61) Shalini, J.; Sankaran, K. J.; Dong, C.-L.; Lee, C.-Y.; Tai, N.-H.; Lin, I.-N. In situ detection of dopamine using nitrogen incorporated diamond nanowire electrode. *Nanoscale* **2013**, *5*, 1159−1167.
(62) Panomsuwan, G.; Saito, N.; Ishizaki, T. Nitrogen-doped carbon nanoparticle−carbon nanofiber composite as an efficient metal-free cathode catalyst for oxygen reduction reaction. *ACS Appl. Mater. Interfaces* **2016**, *8*, 6962−6971.
(63) Khan, I. A.; Qian, Y.; Badshah, A.; Nadeem, M. A.; Zhao, D. Highly porous carbon derived from MOF-5 as a support of ORR electrocatalysts for fuel cells. *ACS Appl. Mater. Interfaces* **2016**, *8*, 17268−17275.
(64) Liu, X.; Xu, G.; Chen, Y.; Lu, T.; Tang, Y.; Xing, W. A strategy for fabricating porous PdNi@ Pt core-shell nanostructures and their enhanced activity and durability for the methanol electrooxidation. *Sci. Rep.* **2015**, *5*, No. 7619.
(65) Prieto, P.; Nistor, V.; Nouneh, K.; Oyama, M.; Abd-Lefdil, M.; Díaz, R. XPS study of silver, nickel and bimetallic silver−nickel nanoparticles prepared by seed-mediated growth. *Appl. Surf. Sci.* **2012**, *258*, 8807−8813.
(66) Singh, B.; Murad, L.; Laffir, F.; Dickinson, C.; Dempsey, E. Pt based nanocomposites (mono/bi/tri-metallic) decorated using different carbon supports for methanol electro-oxidation in acidic and basic media. *Nanoscale* **2011**, *3*, 3334−3349.
(67) Sing, K. S. Reporting physisorption data for gas/solid systems with special reference to the determination of surface area and porosity (Recommendations 1984). *Pure Appl. Chem.* **1985**, *57*, 603−619.
(68) Joo, S. H.; Choi, S. J.; Oh, I.; Kwak, J.; Liu, Z.; Terasaki, O.; Ryoo, R. Ordered nanoporous arrays of carbon supporting high dispersions of platinum nanoparticles. *Nature* **2001**, *412*, 169−172.

DOI: 10.1021/acsomega.9b02741
ACS Omega 2020, 5, 2123−2132